ACS OMEGA

Open Access

http://pubs.acs.org/journal/acsodf

Article

Palmyrah Seed-Derived Activated Charcoal/TiO_2 Composites as a Counter Electrode for Dye-Sensitized Solar Cells

Tharmakularasa Rajaramanan,* Muthugalage Ishara Umayangani Weerasinghe, Gamaralalage Rajanya Asoka Kumara, Meena Senthilnanthanan, Punniamoorthy Ravirajan, and Dhayalan Velauthapillai*

Cite This: *ACS Omega* 2025, 10, 39415−39425

Read Online

ACCESS | Metrics & More | Article Recommendations | Supporting Information

ABSTRACT: Platinum (Pt) is a widely used counter electrode (CE) material in dye-sensitized solar cells (DSSCs) due to its excellent catalytic properties. However, the steep cost limits its widespread adoption. This has spurred researchers to focus on carbon-based materials, which are abundant and economically viable alternatives. In this study, charcoal was derived from palmyrah seeds and activated by a simple thermal shock method involving rapid water immersion. This palmyrah seed-based activated charcoal (AC) was then combined with TiO_2 to create a novel composite paste, enhancing amalgamation between carbon particles and adhesion of the carbon particles on the FTO glass substrate. XPS analysis confirmed the successful formation of the palmyrah seed-derived charcoal. Raman spectroscopic analysis revealed that the palmyrah seed-based AC showcases a graphite nature, a trait retained even in the composite film formed with TiO_2. A DSSC was fabricated employing the as-prepared AC/TiO_2 composite as the CE, N719 dye-coated TiO_2 as the photoanode and an I^-/I_3^- redox couple as the electrolyte. While the optimized AC/TiO_2 (80:20) composite CE annealed at 400 °C demonstrated a power conversion efficiency (PCE) of 4.85%, an encouraging result relative to the PCE of a commercial Pt CE (6.88%), the AC/TiO_2 composite offers a cost-effective and eco-friendly alternative, with potential for future optimization. Moreover, the device with the AC/TiO_2 composite CE displayed notable catalytic reduction of I_3^- to I^- and greatest stability compared to the DSSC fabricated with Pt CE.

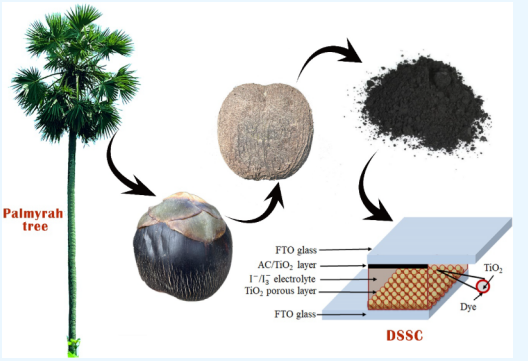

1. INTRODUCTION

Dye-sensitized solar cells (DSSCs) are an emerging photovoltaic technology known for their low-cost production and efficient solar energy conversion potential.[1] A typical DSSC includes a transparent electrode with a dye-coated metal oxide film, a redox electrolyte, and a counter electrode (CE) that is often platinum-based.[2] In DSSCs, continuous advancements have been made by systematically analyzing and optimizing each component to enhance the PCE. A DSSC utilizing an I^-/I_3^- redox couple electrolyte, a C106 (Ru complex) sensitizer, and a Pt CE demonstrated a PCE of 11.7%.[3] In a separate study, a DSSC using the same I^-/I_3^- electrolyte and Pt CE, but sensitized with XW61 (D−π−A structure, organic and porphyrin dye) with coadsorbents, achieved an even higher PCE of 12.4%.[4] Subsequent modifications have demonstrated significant improvements in the photovoltaic performance. For instance, replacing the electrolyte, sensitizer, and CE with a Co^{3+}/Co^{2+} redox couple, a porphyrin-based dye (SM315), and graphene nanoplatelets, respectively, resulted in an increased PCE of 13.0%.[5] Similarly, Ren et al. reported an outstanding PCE of 15.2% by employing a Cu^{2+}/Cu^{+} redox couple, SL9 + SL10 (organic D−π−A structure) sensitizer, and a PEDOT-based CE.[6] These findings underscore the crucial role of each DSSC component in determining the overall device efficiency.

In particular, the CE plays a critical role in facilitating charge transfer between the electrolyte and the electrode interface, while minimizing the recombination of I_3^- ions with the electrons in the conduction band of TiO_2.[7] Moreover, a good CE material should possess superior catalytic activity, electrical conductivity, and chemical stability as it acts as a catalyst to reduce the redox electrolyte by injecting electrons for subsequent regeneration of the dye molecules.[8] Although Pt is highly effective as a catalyst, its high cost and energy-intensive fabrication process limit its scalability in DSSCs.[9−11] Furthermore, the high cost of Pt due to its rarity, complex extraction process, and high demand contributes significantly to the overall cost of DSSCs with the Pt CE alone accounting

Received: November 1, 2024
Revised: July 10, 2025
Accepted: July 18, 2025
Published: August 27, 2025

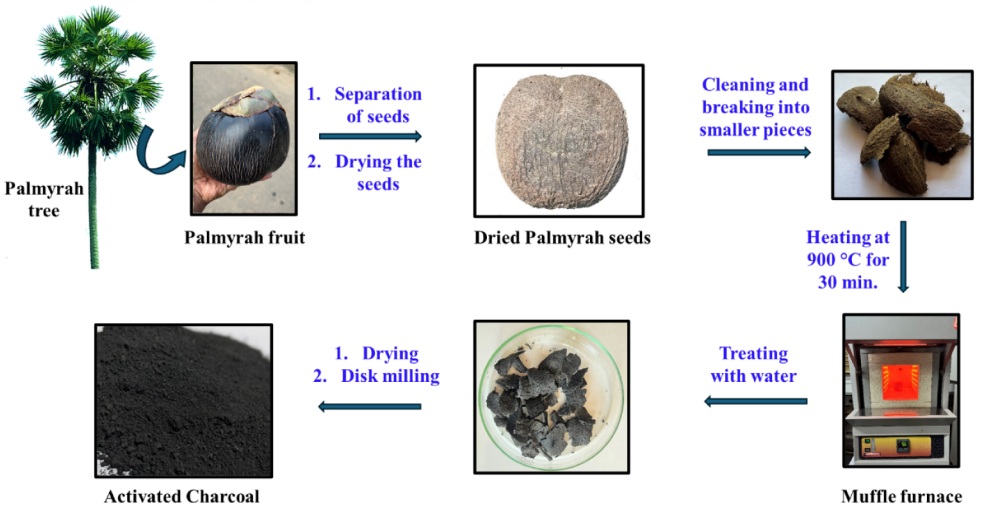

Figure 1. Schematic illustration of the AC prepared from palmyrah seeds.

for nearly 50% of the total device cost.[12] The limited availability of Pt further exacerbates the challenge of meeting the growing demand for its diverse applications.

In response to Pt's limitations, research has focused on low-cost carbon-based alternatives. The carbon-based materials are among the most promising alternatives, which offer a cost-effective solution without compromising performance. Various carbon materials, including carbon black,[13] graphite,[14] hard carbon spherule,[15] carbon nanotubes,[16] graphene,[17] and carbon derived from sources like sucrose[18] and glucose,[19] have been successfully employed as CEs in DSSCs. These materials exhibit excellent conductivities and high surface areas, resulting in DSSC efficiencies comparable to those achieved with Pt CEs, but at a fraction of the cost.[20] Additionally, some studies have reported the successful preparation of charcoal from natural sources and excellent photovoltaic performance exhibited by DSSCs consisting of charcoal-based CEs.

For instance, Cha et al. utilized alkali-treated fallen leaves of the quince plant to prepare honeycomb-like porous carbon for CE, achieving a power conversion efficiency (PCE) of 5.52%.[21] Kumarasinghe et al. developed a CE with highly conductive activated charcoal from coconut shells via thermal shock treatment, yielding a DSSC with an impressive PCE of 7.85%.[22] Similarly, Jiang et al. prepared highly ordered mesoporous carbon arrays through carbonization of natural bamboo and oak wood slices in an argon (Ar) atmosphere and used them directly as CEs, with the devices achieving PCEs of 4.53% for bamboo-based mesoporous carbon arrays and 7.98% for oak-based mesoporous carbon arrays.[23]

A common challenge when using charcoal materials is the low amalgamation of carbon particles and poor adhesion between the carbon particles and the FTO glass substrate. To improve carbon particle cohesion and adhesion on substrates, TiO_2 has been used effectively as a binder.[24] In a separate study, Don et al. incorporated TiO_2 as a binder in an acetylene carbon black/graphite composite CE, achieving a PCE of 5.9%, which is comparable to that of Pt-based DSSCs (PCE = 6.2%).[25] Similarly, Younas et al. used TiO_2 as a binder in a multiwalled carbon nanotube (MWCNT)-based CE, achieving a PCE of 6.65%.[26] Sigdel et al. employed an electrospun carbon nanofiber/TiO_2 nanoparticle composite as a CE for DSSC and obtained a PCE of 7.57%.[24]

In this study, we developed a counter electrode for DSSCs using activated charcoal from palmyrah seeds combined with TiO_2, offering a sustainable, cost-effective alternative to platinum. The palmyrah tree, symbolic to Northern Sri Lanka and known for its sustainable uses, provides a novel source for carbon-based materials in clean energy applications

2. MATERIALS AND METHODS

2.1. Materials. Absolute ethanol (>99%), acetic acid (99.8%), *tert*-butanol (≥99.7%, GC), acetonitrile (gradient grade, ≥99.9), and ditetrabutylammonium *cis*-bis-(isothiocyanato)bis(2,2′-bipyridyl-4,4′-dicarboxylato)-ruthenium(II) dye (*N*-719, 95%) were obtained from Sigma-Aldrich. Titanium tetraisopropoxide (98+%) was sourced from Thermo Scientific, and Triton X-100 was acquired from Acros Organics. Palmyrah seeds were collected in Jaffna, Sri Lanka.

2.2. Preparation of Activated Palmyrah Seed-Based Charcoal Powder. Palmyrah seed-based AC was prepared by using a facile method. Initially, the fibers on the surface of the palmyrah seeds were removed using sandpaper. The seeds were then broken into small pieces and washed with distilled water. After being cleaned, the pieces were dried in natural sunlight. The cleaned and dried Palmyrah seeds were physically activated by heating at 900 °C for 30 min in a box furnace followed by instantly dropping the hot charcoal into a distilled water tank. This activation process was repeated twice more, and the resultant activated charcoal pieces were dried and milled into a powder (Figure 1).

2.3. Preparation Photoanode. The photoanode of the DSSC was prepared as reported elsewhere.[22] Fluorine-doped tin oxide (FTO)-coated glass substrates (sheet resistance 7 Ω/cm^2) were first cleaned with soap water, followed by distilled water and ethanol. The cleaning process was carried out in an ultrasonic bath for 10 min with each cleaning agent, after which the substrates were dried using a hair dryer. To prepare the TiO_2 colloidal solution, 1.0 mL of acetic acid and 8.0 mL of ethanol were added to 8.0 mL of titanium tetraisopropoxide and stirred for 15 min. Steam was then passed through the mixture to promote rapid hydrolysis. The resulting TiO_2 solid was ground with 20.0 mL of deionized water using a mortar, followed by 10 min of sonication. The resulting dispersion was transferred into a Teflon-lined stainless-steel autoclave, where the hydrothermal reaction occurred at 150 °C for 3 h. After the

https://doi.org/10.1021/acsomega.4c09967
ACS Omega 2025, 10, 39415−39425

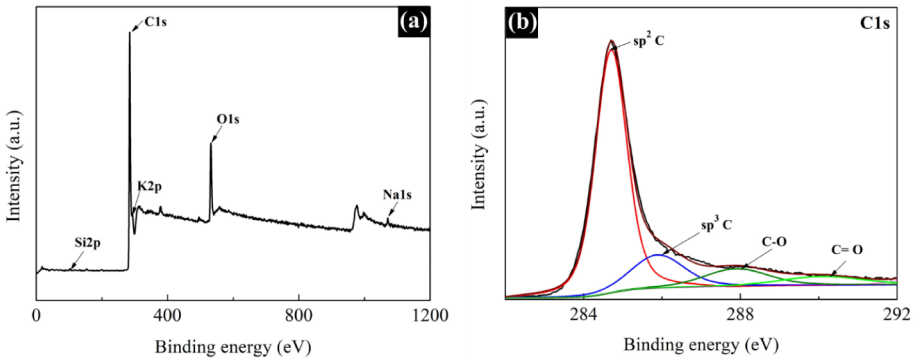

Figure 2. (a) Wide-scan XPS spectrum of palmyrah seed-based AC powder and (b) high-resolution XPS spectrum of C 1s.

reaction, the autoclave was allowed to cool naturally to room temperature. The TiO_2 colloidal solution was then mixed with 30.0 mL of ethanol, 8.25 mL of acetic acid, and 0.4 mL of Triton X-100 to obtain a well-dispersed TiO_2 precursor. This suspension was sprayed onto preheated (150 °C) FTO glass substrates. The TiO_2-coated substrates were subsequently annealed at 500 °C for 30 min in a muffle furnace (average TiO_2 particle size is 14.34 nm). The annealed TiO_2-coated glasses were then immersed overnight in a 0.3 mM solution of N719 dye dissolved in a mixture of acetonitrile and *tert*-butyl alcohol (50% v/v). Following the dye-sensitization process, the photoanodes were rinsed with acetonitrile to remove any unanchored dye molecules and dried.

2.4. Preparation of the Counter Electrode. Five different palmyrah seed-based AC/TiO_2 composites were prepared by mixing palmyrah seed-based AC and TiO_2 in varied ratios (50:50, 60:40, 70:30, 80:20, and 90:10) with Triton X-100 and ethanol. Then, the corresponding composite pastes were individually coated on the FTO glass by a doctor-blade method and annealed at 200 °C to obtain the respective CEs. A control CE was prepared by utilizing the palmyrah seed-based AC only.

2.5. Fabrication of DSSCs. The DSSCs were fabricated by assembling the dye-coated TiO_2 photoanode, the as-prepared CE (consisting of either AC/TiO_2, AC, or Pt), and the I^-/I_3^- electrolyte. Furthermore, the palmyrah seed-based AC/TiO_2 (80:20) composite was employed as CE, and devices were fabricated by varying the CE thickness (1−4 layers) and annealing temperature (200 to 500 °C). The DSSCs had an area of 1 cm^2, and a 0.25 cm^2 mask was used during measurements to define the effective area, minimizing the impact of light scattering.

2.6. Characterization of the Synthesized Nanomaterials. The structural properties of the synthesized AC were studied using XPS analysis, performed with the Thermo Scientific ESCALAB Xi instrument (Thermo Fisher Scientific, Waltham, MA, USA) with Al Kα as the X-ray source. X-ray diffraction (XRD) analysis was performed using a PANalytical AERIS instrument (Almelo, Netherlands). The diffraction pattern was collected with Cu Kα radiation (λ = 1.5408 Å) under ambient temperature under the following operational conditions: an accelerated voltage of 40 kV, an emission current of 44 mA, a scan range (2θ) from 10° to 90°, and a step size of 0.0027°. Raman spectroscopy was carried out using a Labram HR800 Horiba spectrometer equipped with an air-cooled CCD detector (ANDOR) and Argon laser radiation (514.5 nm). The surface morphology was analyzed using a field-emission scanning electron microscope (FE-SEM, ZEISS, SIGMA, UK). The nitrogen adsorption−desorption isotherms were performed using a Quantachrome Autosorb IQ analyzer with ASiAwin software. The photovoltaic performance of the cells was studied using a Keithley-2400 source measurement unit (SMU) under simulated irradiation by a 150 W Xe lamp with an intensity of 100 mW cm^{-2} with AM 1.5 filter (Peccell-PEC-L12, Kanagawa, Japan), and the effective area of the device was maintained at 0.25 cm^2. Electrochemical impedance spectroscopy (EIS) and chronoamperometry measurements were performed using an SP-150 electrochemical workstation (Biologic Science Instruments) through a two-electrode electrochemical setup. Cyclic voltammetry analysis was performed by using an SP-150 electrochemical workstation with a three-electrode system. AC/TiO_2, AC, and Pt served as the working electrodes, while an Ag/AgCl (KCl saturated) electrode and a Pt electrode were used as the reference and counter electrodes, respectively. The incident photon-to-current efficiency (IPCE) spectrum was recorded using a Bentham TMc300 monochromator.

3. RESULTS AND DISCUSSION

3.1. Structural Studies. *3.1.1. Structural Study of Palmyrah Seed-Based AC.* To investigate the elemental composition and chemical bonding states of the synthesized AC, X-ray photoelectron spectroscopy (XPS) was carried out. The wide-scan spectrum (Figure 2a) reveals dominant peaks corresponding to C 1s (85.8 at. %) and O 1s (12.3 at. %), confirming that carbon and oxygen are the major constituents of the charcoal. Minor peaks attributed to K 2p, Si 2p, and Na 1s were also detected, likely originating from residual inorganic elements present in the biomass precursor or introduced during activation processes.

The high-resolution core-level spectrum of C 1s was deconvoluted into four Gaussian peaks, corresponding to sp^2 carbon (sp^2 C), sp^3 carbon (sp^3 C), C−O, and C═O bonding states.[27] As illustrated in Figure 2b, the main peak at 284.7 eV (53.4 at. %) is attributed to sp^2-hybridized graphitic carbon. This graphitic structure enhances electrical conductivity, which is essential for efficient electron transfer when used as a CE in DSSCs. The peak at 285.9 eV (12.3 at %) corresponds to sp^3-hybridized carbon, which indicates structural defects and surface functionalization.[28] These disordered carbon domains contribute to increased porosity and surface roughness,[29] thereby enhancing the electrochemically active surface area and facilitating better interaction with the electrolyte. The peaks observed at 287.9 eV (7.9 at %) and 290.1 eV (5.0 at %) are assigned to C−O and C═ O functional groups, respectively. The presence of these oxygen-containing groups

https://doi.org/10.1021/acsomega.4c09967
ACS Omega 2025, 10, 39415−39425

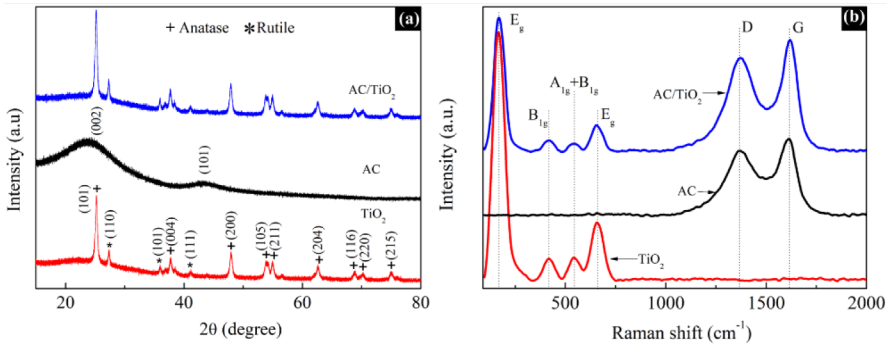

Figure 3. (a) XRD patterns and (b) Raman spectra of the AC/TiO_2, AC, and TiO_2 films.

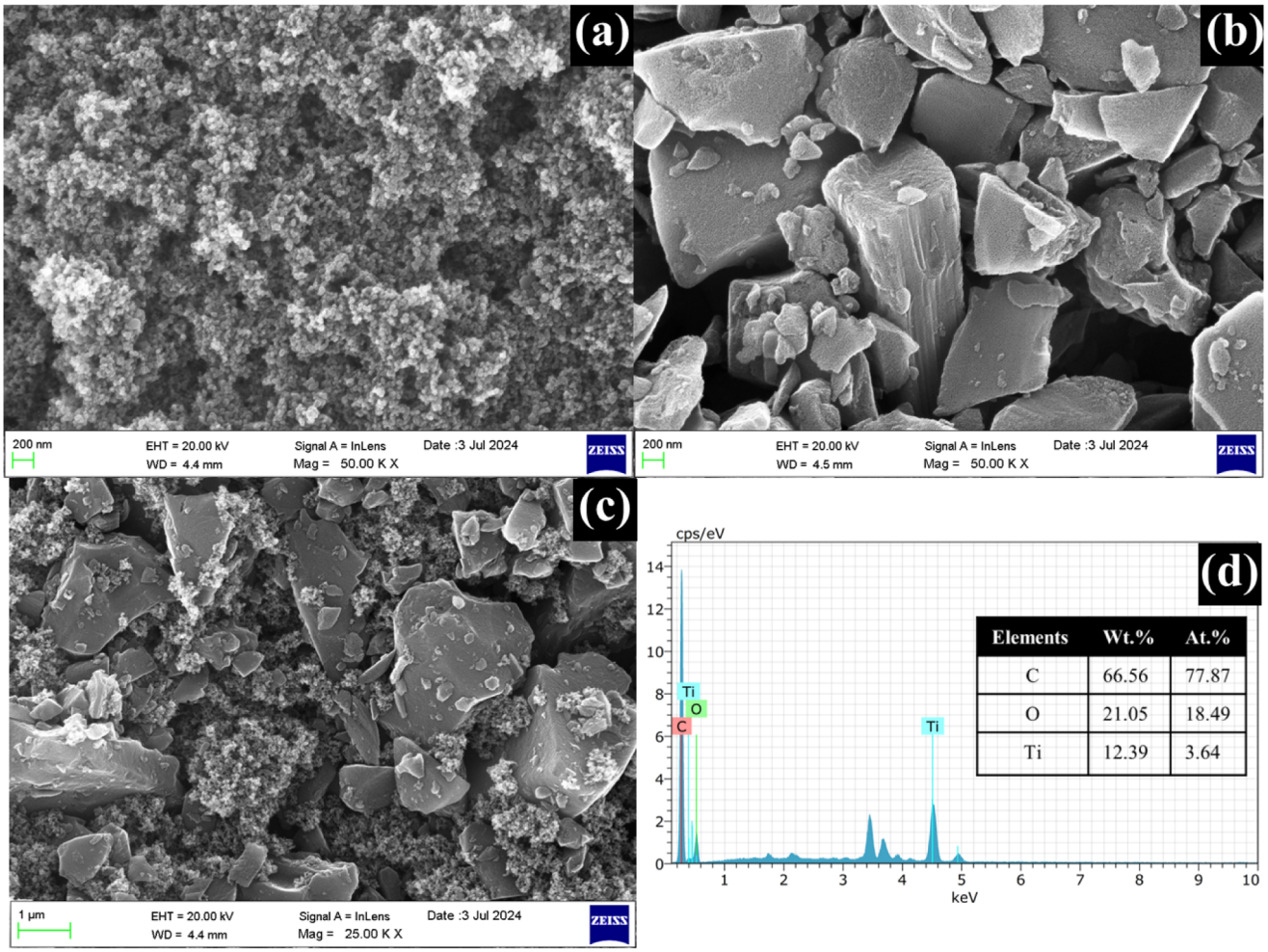

Figure 4. FE-SEM images of (a) TiO_2, (b) AC, (c) AC/TiO_2 films, and (d) EDX spectrum of the AC/TiO_2 film.

indicates surface oxygenation, which plays a dual role in improving the electrocatalytic performance. First, these groups can act as active sites for the reduction of triiodide (I_3^-) in the electrolyte,[30] mimicking the catalytic behavior of platinum-based electrodes. Second, they enhance the hydrophilicity of the carbon surface, promoting better contact with the liquid electrolyte and thus improving charge transfer kinetics.[31] Therefore, the XPS analysis confirms that the prepared AC powder possesses a favorable combination of graphitic domains for electrical conductivity and oxygen-functional groups for catalytic activity, making it a promising candidate for use as a CE in DSSCs.

3.1.2. Structural Study of Prepared AC, AC/TiO_2, and TiO_2 Films. The structural properties of the prepared AC, AC/TiO_2, and TiO_2 films were analyzed by XRD. The XRD analysis, illustrated in Figure 3a, shows two broad bands centered at 23.73° and 43.67° corresponding to the reflection planes of (002) and (100), respectively, and confirms successful formation of the AC.[32] The appearance of these broad bands in a wide-angle range and the absence of sharp peaks reveal poor crystallinity of the AC material.[33] For the AC/TiO_2 composite, the relative intensity of the (101) peak of TiO_2 increases due to the overlapping of the diffraction intensity of

https://doi.org/10.1021/acsomega.4c09967
ACS Omega 2025, 10, 39415−39425

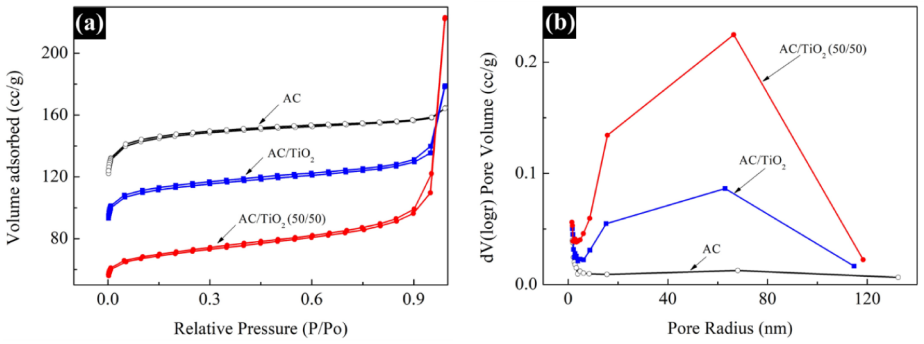

Figure 5. (a) Nitrogen adsorption−desorption isotherms and (b) BJH pore-size distributions of the AC, AC/TiO_2 (80:20), and AC/TiO_2 (50:50) films.

the (002) peak of AC with that of the (101) peak of TiO_2 which confirms the composite formation.

Raman spectroscopic measurements were taken to further confirm the formation of AC and AC/TiO_2 composite as indicated in Figure 3b. The presence of well-resolved Raman peaks with the D_{4h} space group at about 168 and 660 cm^{-1} (E_g), 545 cm^{-1} (A_{1g} + B_{1g}), and 422 cm^{-1} (B_{1g}) corresponding to the anatase phase of TiO_2 are in consistent with the values reported in the literature.[2] Furthermore, AC and AC/TiO_2 composite exhibit two characteristic peaks located at about 1366 and 1616 cm^{-1} corresponding to disorder carbon (D-band) and graphite carbon (G-band), respectively.[34] Generally, the G-band is attributed to stretching of the bond between sp^2 hybridized carbon atoms (E_{2g} vibrational mode), while the D-band represents the defect sites associated with vacancies and grain boundaries.[35] It is noteworthy to mention that the ratio of peak intensities between the aforementioned bands (ID/IG) is crucial to estimate the structural disorder of carbon sheets.[36] The trend observed in these peak intensities also correlates well with the XPS results. In the present study, the ID/IG ratio was found to be 0.84 for both AC and the AC/TiO_2 composite. As this ratio is less than one, it clearly demonstrates that the palmyrah seed-based AC is mostly of graphitic nature, which is retained in the composite as well.

3.2. Morphological Study. Surface morphologies of the AC/TiO_2, AC, and TiO_2 films were studied by field emission scanning electron microscopy (FE-SEM), and the images are displayed in Figure 4.

The SEM image of TiO_2 exhibits spherical particles (Figure 4a) while that of AC shows irregular shapes and sizes (Figure 4b). Figure 4c illustrates the SEM image of the AC/TiO_2 composite film demonstrating successful formation of the composite in a homogeneous manner. The adsorption capacity of AC is primarily influenced by its porosity and the chemical reactivity of functional groups present on its surface. As shown in the SEM images, both AC alone and the AC/TiO_2 composite consist of large and small aggregates with numerous pores. This porous structure results in a significantly larger surface area, which enhances electrolyte adsorption and subsequently catalyzes the redox reaction between I^- and I_3^- ions in the electrolyte. Furthermore, the I^-/I_3^- electrolyte tends to evaporate easily under open device conditions. However, this evaporation is minimized when AC holds I^-, I_3^- ions, and electrolyte solvents within its pores. The elemental composition of the AC/TiO_2 composite was analyzed using energy-dispersive X-ray spectroscopy (EDX). The EDX spectrum of the composite film reveals the presence of C, O, and Ti, further confirming the formation of the composite (Figure 4d). The peak observed between 3 and 4 keV corresponds to the Sn element in the FTO substrate. Furthermore, the high carbon content observed in the EDX spectra of AC and AC/TiO_2 composite films confirms that the prepared AC is of high purity (Figures S1 and 4d).

3.3. BET and BJH Analysis. The nitrogen adsorption−desorption isotherms provide valuable insights into the textural characteristics of the materials. To evaluate the effect of TiO_2 incorporation on the surface area and pore structure of activated carbon (AC), BET and BJH analyses were conducted on AC, the optimized AC/TiO_2 (80:20) composite, and the higher TiO_2-loaded AC/TiO_2 (50:50) composite films (Figure 5).

The nitrogen adsorption−desorption measurements reveal a clear trend in the surface area and porosity of the AC/TiO_2 composites as the TiO_2 content increases. The AC exhibits the highest BET surface area of 479.48 m^2/g, which gradually decreases to 368.63 m^2/g for the AC/TiO_2 (80:20) composite and further to 233.17 m^2/g for the AC/TiO_2 (50:50) composite (Table 1). This decline in surface area is likely due to partial blockage or coverage of micropores by TiO_2 nanoparticles, reducing access to internal carbon surfaces.[37] Despite the reduction in surface area, a notable increase in total pore volume is observed, from 0.25 cc/g for AC to 0.28 and 0.35 cc/g for the 80:20 and 50:50 composites, respectively (Table 1). This suggests that the inclusion of TiO_2 not only modifies the pore structure but also contributes to the formation of new void spaces or interparticle porosity within the composite matrix.

Table 1. BET and BJH Parameters of the AC, AC/TiO_2 (80:20), and AC/TiO_2 (50:50) Films

Samples	BET Surface Area (m^2/g)	Total Pore Volume (cc/g)	BJH Surface Area (m^2/g)
AC	479.48	0.25	13.11
AC/TiO_2 (80:20)	368.63	0.28	20.85
AC/TiO_2 (50:50)	233.17	0.35	28.93

Interestingly, the BJH surface area, which reflects the mesoporous contribution, increases consistently with TiO_2 loading from 13.11 m^2/g (AC) to 20.85 m^2/g (80:20) and 28.93 m^2/g (50:50) (Table 1). The improved mesoporosity is advantageous for electrochemical applications, as it enhances electrolyte diffusion and ion transport, particularly in DSSCs.[38] These results suggest that while excessive TiO_2 may reduce the

https://doi.org/10.1021/acsomega.4c09967
ACS Omega 2025, 10, 39415−39425

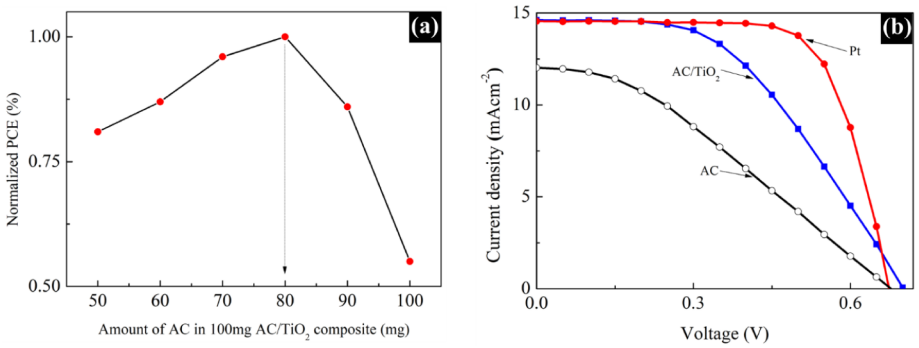

Figure 6. (a) Influence of the amount of AC in the AC/TiO_2 composite on PCE. (b) J−V measurements of AC/TiO_2, AC, and Pt CEs-based DSSCs.

overall surface area, it simultaneously enhances the mesoporous structure and pore volume, which could promote better catalytic activity at the electrode/electrolyte interface. Therefore, a balanced ratio such as AC/TiO_2 (80:20) may offer an optimal trade-off between electrical conductivity (from charcoal) and catalytic accessibility (supported by TiO_2 and mesoporosity), making it a promising counter electrode material for DSSCs.

3.4. Photovoltaic Study. The photovoltaic performance of the fabricated DSSCs with different CEs was evaluated by typical I−V characteristic study under simulated irradiation with an intensity of 100 mW cm^{-2} using an AM 1.5 filter. As indicated in Figure 6a, various AC/TiO_2 composites were analyzed, and optimal photovoltaic performance was achieved for the composite consisting of 80 mg of AC and 20 mg of TiO_2. In the subsequent study, the thickness of the AC/TiO_2 (80:20) composite CE was varied from one to four layers using Scotch tape and annealed at 200 °C. As the CE thickness was increased, all photovoltaic parameters declined due to an increase in total resistance. The best PV performance was obtained when the CE thickness was two layers of Scotch tape (Figure S2 and Table S1).

Then, the annealing temperature of the two-layered AC/TiO_2 (80:20) composite CE was varied from 200 to 500 °C. At lower annealing temperatures, reduced porosity and incomplete evaporation of the Triton X-100 binder resulted in decreased PCEs of the corresponding devices. Studies report that at low substrate temperatures, excess binder remains in the CE material, increasing resistance in the charcoal-based CE and reducing efficiency.[22] In a separate study, low annealing temperatures were found to reduce porosity and spacing between TiO_2 particles in the TiO_2 film.[39] The AC in the said CE began to ash at 500 °C, further diminishing the PCE. Hence, this study reveals the optimal PV performance at an annealing temperature of 400 °C (Figure S3 and Table S2). Figure 6b and Table 2 illustrate the comparison of photovoltaic performances of DSSCs fabricated with AC/TiO_2 composite, AC, and Pt counter electrodes. A promising PCE of 4.85% was achieved for the device consisting of the AC/TiO_2 (80:20) composite CE, representing a slight reduction compared with the Pt CE-based device (PCE = 6.88%).

Table 2. Photovoltaic Parameters of the AC/TiO_2, AC, and Pt CE-Based DSSCs

Counter Electrode	J_{SC} (mA cm^{-2})	V_{OC} (V)	FF	PCE (%)
AC/TiO_2 (80:20)	14.61	0.70	0.47	4.85
AC	12.01	0.67	0.33	2.69
Pt	14.54	0.67	0.70	6.88

The DSSC fabricated with the AC/TiO_2 (80:20) composite CE shows slightly higher V_{OC} and J_{SC} values and lower fill factor compared with the platinum-based device. As the AC/TiO_2 composite CE is shown to possess greater porosity and surface area than Pt CE, formation of the reduced iodide species (I^-) could have been facilitated, thus accelerating the number of photogenerated electrons by the sensitizer dye which could have led to an overall increase in J_{SC}. Poor adhesion of AC/TiO_2 particles on FTO compared to Pt could be attributed to the reduction in FF due to the increased series resistance for the AC/TiO_2 CE-based device.

When the AC alone (without TiO_2) was used as the CE, the corresponding device exhibited the lowest J_{SC}, V_{OC}, and FF values. This could be attributed to the lack of amalgamation between carbon particles and poor adhesion of the carbon particles on the FTO glass substrate, which could have led to higher recombination rate and internal resistance of the device (Figure 7).

3.5. EIS Analysis. Electrochemical impedance spectroscopy (EIS) is a powerful tool which reveals the inherent electrochemical behavior and the interfacial charge transfer process of the DSSC. EIS analysis was carried out in the frequency range from 10^{-2} to 10^6 Hz with 0.70 V forward bias under dark conditions on the fabricated devices to study the effect of interfacial resistance on the device performance, and the results are illustrated in Figure 8a. The respective interfacial resistance values for each device were extracted from the equivalent circuit, and the results are displayed inside Figure 8a.

A typical EI spectrum of a DSSC consists of three semicircles. The largest semicircle in the midfrequency range corresponds to the charge transport resistance at the photoanode/electrolyte interface, known as the recombination resistance under dark conditions (R_{rec}).[40,41] The third semicircle in the low-frequency range represents the Warburg diffusion process of the I^-/I_3^- redox couple in the electrolyte (Z_w) while the first semicircle in the high-frequency region is associated with the charge transfer resistance at the counter electrode/electrolyte interface (R_{ct}).[2] The intercept of the first semicircle on the X-axis represents the series resistance (R_S), which is related to the intrinsic resistance of the assembled cell.[42]

In the present study, the photoanode/electrolyte interface condition remains the same for all three devices based on different CEs. Further, the Warburg diffusion process could not be clearly resolved in this analysis. It should be noted that

https://doi.org/10.1021/acsomega.4c09967
ACS Omega 2025, 10, 39415−39425

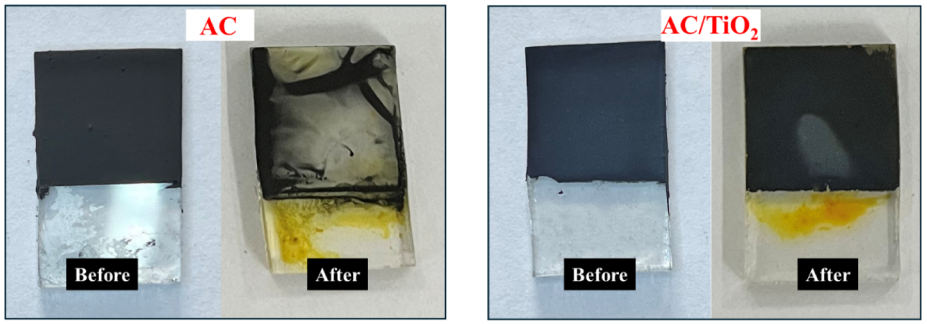

Figure 7. AC and AC/TiO_2 CEs before and after the fabrication of DSSCs.

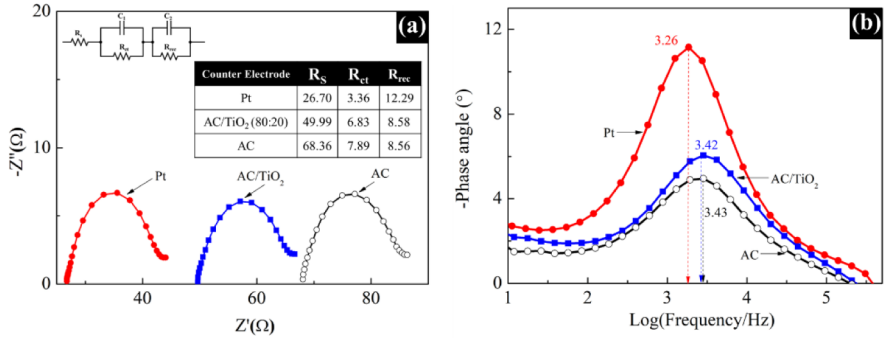

Figure 8. (a) Electrochemical impedance spectroscopy (Nyquist plots) and (b) Bode plot for DSSC with AC/TiO_2, AC, and Pt CEs.

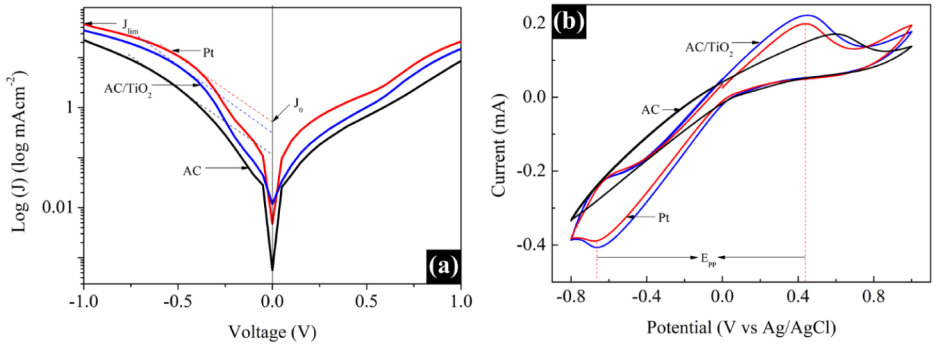

Figure 9. (a) Tafel polarization curves. (b) Cyclic voltammogram for AC/TiO_2, AC, and Pt CEs.

R_{ct} is inversely proportional to the catalytic ability of the CE to reduce I_3^- to I^- species. The AC/TiO_2 composite CE exhibits a higher R_{ct} value compared to the Pt CE but a lower R_{ct} than the AC CE. This indicates that the AC/TiO_2 composite catalyzes the reduction of I_3^- to I^- more efficiently than AC but less effectively than Pt. As a result, the improved catalytic activity of the AC/TiO_2 composite CE plays a significant role in enhancing the J_{SC} value observed in the J−V measurements.[25] Moreover, it is well known that the FF in a DSSC is strongly influenced by R_S; thus, minimizing R_S is critical to achieve a higher FF.[25] The elevated R_S values observed for the DSSCs with AC and AC/TiO_2 composite CEs confirm poor adhesion of the particles to the FTO substrate.[20] The trend in R_S values aligns with the FF values obtained from the J−V measurements, further corroborating the EIS data with the photovoltaic performance results. The R_{rec} value is higher for the Pt CE device, which could contribute to improved V_{OC}. However, in our study, R_{rec} does not significantly limit the overall device performance. Figure 8b presents the Bode plots of devices with all three counter CEs. The electron lifetime (T_e), also known as the charge recombination time under dark conditions, was estimated using the following equation:

$$T_e = \frac{1}{2\pi f_{max}} \quad (1)$$

where f_{max} is the maximum frequency corresponding to the peak.[43] In this study, the calculated charge recombination times were 48.82, 46.53, and 46.40 ms for Pt, AC/TiO_2, and AC, respectively. A higher charge recombination time reduces the recombination rate, thereby improving the V_{OC}. However, in our study, no significant variations in the charge recombination time were observed among the devices with different CEs, which explains the unchanged V_{OC} values in the J−V measurements.

3.6. Electrocatalytic Analysis. The electrocatalytic activities of the AC/TiO_2, AC, and Pt electrodes in DSSCs were analyzed using Tafel polarization measurements, as shown in Figure 9a. For these measurements, complete DSSCs were fabricated with each CE separately, and J−V measurements were conducted under dark conditions. The

https://doi.org/10.1021/acsomega.4c09967
ACS Omega 2025, 10, 39415−39425

data were then converted to Tafel polarization curves by plotting the logarithmic value of the absolute current density (J) as a function of voltage (V). The limiting diffusion current density (J_{lim}) is positively correlated with the diffusion coefficient, reflecting the diffusion behavior of the I^-/I_3^- redox couple in the electrolyte.[44] The slope of the Tafel curve represents the exchange current density (J_0), which can be expressed by the following equation:

$$J_0 = \frac{RT}{nFR_{ct,Tafel}} \quad (2)$$

where $R_{ct,Tafel}$ is the charge transfer resistance from Tafel polarization, R is the gas constant, F is the Faraday constant, T is the absolute temperature, and n is the number of electrons involved in the reaction. $R_{ct,Tafel}$ is inversely proportional to J_0,[45] meaning a higher J_0 corresponds to a lower $R_{ct,Tafel}$, indicating superior electrocatalytic activity. The $R_{ct,Tafel}$ values follow the order: AC > AC/TiO_2 > Pt, confirming that Pt exhibits the highest electrocatalytic activity. However, compared to AC, the AC/TiO_2 composite demonstrates significantly improved electrocatalytic performance. This trend is consistent with the R_{ct} values obtained from the EIS analysis.

To further evaluate the electrocatalytic activity of the CEs, cyclic voltammetry (CV) was performed, and the results are presented in Figure 9b. The analysis was conducted using AC/TiO_2, AC, and Pt CEs in an I^-/I_3^- electrolyte containing 10 mM LiI and 1 mM I_2 in acetonitrile solution.[46] The measurements were carried out at a scan rate of 100 mV s^{-1} to investigate the electrocatalytic activity of the samples within the potential range of −0.8 to 1 V. In CV curves, the potential at which the oxidation peak occurs is referred to as the anodic peak potential (E_{pa}), while the potential at which the reduction peak occurs is known as the cathodic peak potential (E_{pc}).

Both oxidation and reduction peaks were clearly observed for the AC/TiO_2 and Pt CEs, while the cathodic peak was not observed in the AC CE, and the AC material was immediately removed from the substrate during the measurement. The difference between the anodic peak potential (E_{pa}) and cathodic peak potential (E_{pc}) is referred to as the peak-to-peak separation (E_{pp}), which is inversely correlated with the standard electrochemical rate constant of the redox reaction and the electrocatalytic ability of the samples.

A slightly lower E_{pp} was observed for Pt compared to AC/TiO_2, indicating that the Pt CE exhibits faster reversibility of the redox reaction or better kinetics. The cathodic peak current density (I_{pc}) and anodic peak current density (I_{pa}) represent the maximum current densities at E_{pc} and E_{pa}, respectively. A higher absolute value of I_{pc} implies better electrocatalytic ability of the material. In contrast, higher values were observed for AC/TiO_2 compared to Pt. The AC/TiO_2 composite has a highly porous structure and active surface sites, which increases the surface area and allows more redox reactions to occur simultaneously, leading to higher peak current densities. Despite its high surface area, the intrinsic catalytic activity of AC/TiO_2 is lower than that of Pt, as Pt has a superior work function and electrical conductivity, resulting in better electrocatalytic performance. Nevertheless, the AC/TiO_2 CE still demonstrated comparable electrocatalytic activity. Figure S4a,b presents the cyclic voltammetry (CV) curves of AC/TiO_2 and Pt CEs at varying scan rates. Similar to Pt, the peak current of AC/TiO_2 increases as the scan rate rises from 50 to 250 mV/s. The linear relationship between peak current and $V^{1/2}$ confirms a diffusion-controlled process, where the movement of electroactive species toward the electrode surface is governed by diffusion rather than surface adsorption or kinetic limitations (Figure S4c,d). Furthermore, the higher peak current observed at elevated scan rates indicates efficient charge transport in the AC/TiO_2 electrode. Additionally, the AC/TiO_2 CE exhibits well-defined and stable redox peaks across different scan rates, demonstrating good electrochemical stability

In summary, AC already possesses a high surface area, but the incorporation of TiO_2 nanoparticles further enhances porosity, providing additional active sites for electrolyte interaction and improving redox reactions at the CE, as illustrated in Figure 10. Moreover, the synergistic effect of

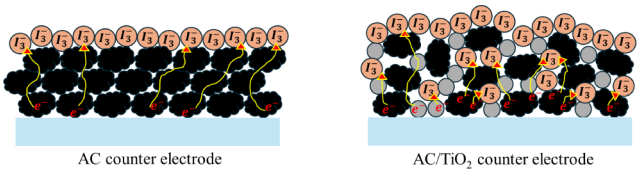

Figure 10. Schematic illustration of the working mechanisms of AC and AC/TiO_2.

TiO_2 and AC plays a crucial role in enhancing the electron transport. TiO_2, known for its excellent electron conductivity, facilitates more efficient charge transfer when combined with AC. Additionally, TiO_2 boosts the catalytic activity of AC, significantly improving the reduction of I_3^- to I^-, thereby enhancing the overall performance of the CE.

3.7. IPCE and Stability Study. The ratio of the electrons generated in the external circuit at a specific wavelength to the incident photons under a short-circuit state is known as the incident photon-to-current efficiency (IPCE) of a dye-sensitized solar cell. The IPCE spectra, measured as a function of wavelength from 300 to 800 nm for the DSSCs with AC/TiO_2 composite, AC, and Pt as CEs are presented in Figure 11a. The integration of the said IPCE curves reveals minimal differences between DSSCs with AC/TiO_2 composite and Pt counter electrodes, both of which exhibit significantly larger areas than the device with AC CE. This observation is consistent with the trend in J_{SC} values obtained from J−V measurements, confirming the superior performance of the AC/TiO_2 composite compared to AC and comparable performance to Pt as CEs.

Stability of the devices with all three CEs was investigated using chronoamperometry by continuously exposing the devices without sealing at 1 sun illumination for 250 s (Figure 11b). DSSCs with AC/TiO_2 composite CE exhibited low current reduction rate compared to a Pt CE based device. This could be attributed to holding more iodide and triiodide ions and preventing evaporation of the electrolyte by the AC/TiO_2 CE based devices due to the presence of high porosity and surface area. In contrast, the electrolyte in Pt CEs can remain on the surface.

4. CONCLUSION

Palmyrah seed-based activated charcoal (AC) was successfully synthesized using a simple method, followed by the fabrication of the counter electrode (CE) consisting of an AC/TiO_2 composite, and its effective application in dye-sensitized solar

https://doi.org/10.1021/acsomega.4c09967
ACS Omega 2025, 10, 39415−39425

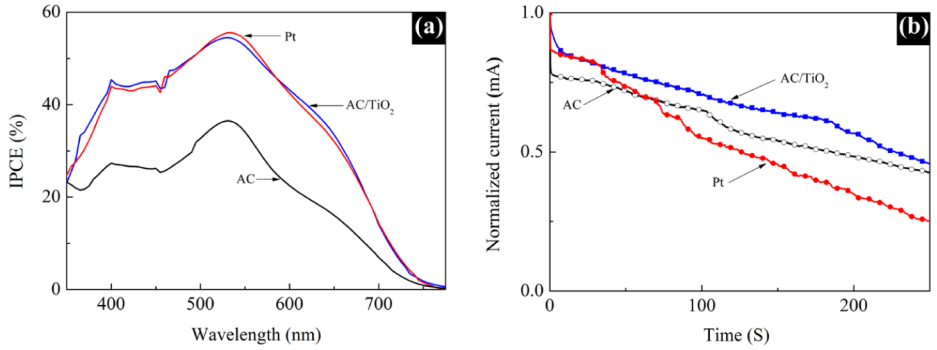

Figure 11. (a) Incident photon-to-current efficiency (IPCE) spectra and (b) stability study of the DSSCs with AC/TiO_2, AC, and Pt CEs.

cells (DSSCs). The synthesized AC powder was analyzed by XPS, while the prepared AC and AC/TiO_2 CEs were characterized by XRD analysis and Raman spectroscopy. The graphite-like structure of the synthesized AC was confirmed by XPS, and this structural nature was retained in both the AC and AC/TiO_2 CEs. Although the power conversion efficiency (PCE) of the AC/TiO_2 composite CE was 4.85% lower than that of the traditional platinum (Pt) CE, the result is promising, demonstrating the AC/TiO_2 CE's viability as a cost-effective, eco-friendly option. Furthermore, EIS and electrocatalytic studies revealed significant catalytic reduction of I_3^- to I^- species by the AC/TiO_2 composite CE compared to the Pt CE. Additionally, the AC/TiO_2 CE demonstrated better stability than the Pt CE under open-device conditions by retaining iodide and triiodide ions due to high porosity and surface area. Hence, the simple fabrication process, notable catalytic reduction of I_3^- to I^- species, better stability, and low cost of the palmyrah seed-based AC/TiO_2 composite CE acts as a promising alternative to the Pt CE used in the existing DSSC applications.

■ ASSOCIATED CONTENT

Supporting Information

The Supporting Information is available free of charge at https://pubs.acs.org/doi/10.1021/acsomega.4c09967.

EDX spectrum of TiO_2 and AC, optimization details of CE thickness and annealing temperature, cyclic voltammograms of AC/TiO_2 and Pt CEs at different scanning rates, as well as the analysis of oxidation and reduction peak currents as a function of the square root of the scanning rate(PDF)

■ AUTHOR INFORMATION

Corresponding Authors

Dhayalan Velauthapillai − *Faculty of Engineering and Science, Western Norway University of Applied Sciences, Bergen 5020, Norway;* orcid.org/0000-0002-4162-7446; Phone: +47-55-87711; Email: Dhayalan.Velauthapillai@hvl.no

Tharmakularasa Rajaramanan − *Department of Physics and Technology, University of Bergen, Bergen 5007, Norway; Faculty of Engineering and Science, Western Norway University of Applied Sciences, Bergen 5020, Norway; Clean Energy Research Laboratory, Department of Physics, University of Jaffna, Jaffna 40000, Sri Lanka;* orcid.org/0000-0003-0351-0439; Phone: +94(0)775572984; Email: rramanan9@gmail.com

Authors

Muthugalage Ishara Umayangani Weerasinghe − *National Institute of Fundamental Studies, Kandy 20000, Sri Lanka*

Gamaralalage Rajanya Asoka Kumara − *National Institute of Fundamental Studies, Kandy 20000, Sri Lanka;* orcid.org/0000-0001-9804-2652

Meena Senthilnanthanan − *Department of Chemistry, University of Jaffna, Jaffna 40000, Sri Lanka*

Punniamoorthy Ravirajan − *Clean Energy Research Laboratory, Department of Physics, University of Jaffna, Jaffna 40000, Sri Lanka*

Complete contact information is available at: https://pubs.acs.org/10.1021/acsomega.4c09967

Author Contributions

T.R.: Conceptualization, Methodology, Data curation, Software, and Writing-Original draft preparation. M.I.U.W.: Methodology and Editing. G.R.A.K.: Conceptualization, Methodology, Investigation, Reviewing, and Editing. M.S.: Data curation, Investigation, Validation, Supervision, Reviewing, and Editing. P.R.: Data curation, Investigation, Validation, Supervision, Visualization, funding acquisition, Reviewing, and Editing. D.V.: Data curation, Investigation, Validation, Supervision, Visualization, funding acquisition, Reviewing, and Editing.

Notes

The authors declare no competing financial interest.

■ ACKNOWLEDGMENTS

This research was funded by Higher Education and Research Collaboration on Nanomaterials for Clean Energy Technologies 2.0 (HRNCET 2.0) project (Grant Number NORPART-2021/10095). The Western Norway University of Applied Sciences, Bergen, Norway provided financial assistance to publish this article with open access. P. Balraju, Coimbatore Institute of Technology, India is hereby acknowledged for FE-SEM & EDX analyses.

■ REFERENCES

(1) Rajaramanan, T.; et al. Natural sensitizer extracted from Mussaenda erythrophylla for dye-sensitized solar cell. *Sci. Rep.* **2023**, *13*, 13844.

(2) Rajaramanan, T.; Velauthapillai, D.; Ravirajan, P.; Senthilnanthanan, M. A facile impregnation synthesis of Ni-doped TiO_2 nanomaterials for dye-sensitized solar cells. *J. Mater. Sci.: Mater. Electron.* **2023**, *34*, 916.

(3) Yu, Q.; et al. High-efficiency dye-sensitized solar cells: The influence of lithium ions on exciton dissociation, charge recombination, and surface states. *ACS Nano* **2010**, *4*, 6032−6038.
(4) Zeng, K.; Chen, Y.; Zhu, W.-H.; Tian, H.; Xie, Y. Efficient solar cells based on concerted companion dyes containing two complementary components: An alternative approach for cosensitization. *J. Am. Chem. Soc.* **2020**, *142*, 5154−5161.
(5) Mathew, S.; et al. Dye-sensitized solar cells with 13% efficiency achieved through the molecular engineering of porphyrin sensitizers. *Nat. Chem.* **2014**, *6*, 242−247.
(6) Ren, Y.; et al. Hydroxamic acid pre-adsorption raises the efficiency of cosensitized solar cells. *Nature* **2023**, *613*, 60−65.
(7) Wu, J.; et al. Counter electrodes in dye-sensitized solar cells. *Chem. Soc. Rev.* **2017**, *46*, 5975−6023.
(8) Sarkar, A.; Bera, S.; Chakraborty, A. K. $CoNi_2S_4$-reduced graphene oxide nanohybrid: An excellent counter electrode for Pt-free DSSC. *Sol. Energy* **2020**, *208*, 139−149.
(9) Özel, F.; Sarılmaz, A.; İstanbullu, B.; Aljabour, A.; Kuş, M.; Sönmezoğlu, S. Penternary chalcogenides nanocrystals as catalytic materials for efficient counter electrodes in dye-synthesized solar cells. *Sci. Rep.* **2016**, *6*, 29207.
(10) Lee, W. J.; Ramasamy, E.; Lee, D. Y.; Song, J. S. Grid type dye-sensitized solar cell module with carbon counter electrode. *J. Photochem. Photobiol., A* **2008**, *194*, 27−30.
(11) Nogueira, A. F.; De Paoli, M.-A. A dye sensitized TiO_2 photovoltaic cell constructed with an elastomeric electrolyte. *Sol. Energy Mater. Sol. Cells* **2000**, *61*, 135−141.
(12) Ahmed, U.; et al. A comprehensive review on counter electrodes for dye sensitized solar cells: A special focus on Pt-TCO free counter electrodes. *Sol. Energy* **2018**, *174*, 1097−1125.
(13) Murakami, T. N.; et al. Highly efficient dye-sensitized solar cells based on carbon black counter electrodes. *J. Electrochem. Soc.* **2006**, *153*, A2255.
(14) Kay, A.; Grätzel, M. Low cost photovoltaic modules based on dye sensitized nanocrystalline titanium dioxide and carbon powder. *Sol. Energy Mater. Sol. Cells* **1996**, *44*, 99−117.
(15) Huang, Z.; et al. Application of carbon materials as counter electrodes of dye-sensitized solar cells. *Electrochem. Commun.* **2007**, *9*, 596−598.
(16) Cha, S. I.; Koo, B. K.; Seo, S. H.; Lee, D. Y. Pt-free transparent counter electrodes for dye-sensitized solar cells prepared from carbon nanotube micro-balls. *J. Mater. Chem.* **2010**, *20*, 659−662.
(17) Roy-Mayhew, J. D.; Bozym, D. J.; Punckt, C.; Aksay, I. A. Functionalized graphene as a catalytic counter electrode in dye-sensitized solar cells. *ACS Nano* **2010**, *4*, 6203−6211.
(18) Kumar, R.; et al. A simple route to making counter electrode for dye sensitized solar cells (DSSCs) using sucrose as carbon precursor. *J. Colloid Interface Sci.* **2015**, *459*, 146−150.
(19) Kumar, R.; Bhargava, P. Fabrication of a counter electrode using glucose as carbon material for dye sensitized solar cells. *Mater. Sci. Semicond. Process.* **2015**, *40*, 331−336.
(20) Kumar, R.; Nemala, S. S.; Mallick, S.; Bhargava, P. Synthesis and characterization of carbon based counter electrode for dye sensitized solar cells (DSSCs) using sugar free as a carbon material. *Sol. Energy* **2017**, *144*, 215−220.
(21) Cha, S. M.; Nagaraju, G.; Sekhar, S. C.; Bharat, L. K.; Yu, J. S. Fallen leaves derived honeycomb-like porous carbon as a metal-free and low-cost counter electrode for dye-sensitized solar cells with excellent tri-iodide reduction. *J. Colloid Interface Sci.* **2018**, *513*, 843−851.
(22) Kumarasinghe, K.; Kumara, G.; Rajapakse, R.; Liyanage, D.; Tennakone, K. Activated coconut shell charcoal based counter electrode for dye-sensitized solar cells. *Org. Electron.* **2019**, *71*, 93−97.
(23) Jiang, Q.; Li, G.; Wang, F.; Gao, X. Highly ordered mesoporous carbon arrays from natural wood materials as counter electrode for dye-sensitized solar cells. *Electrochem. Commun.* **2010**, *12*, 924−927.
(24) Sigdel, S.; et al. Dye-sensitized solar cells based on spray-coated carbon nanofiber/TiO_2 nanoparticle composite counter electrodes. *J. Mater. Chem. A* **2014**, *2*, 11448−11453.
(25) Don, M. F.; Ekanayake, P.; Nakajima, H.; Mahadi, A. H.; Lim, C. M. Improvement of dye-sensitized solar cell performance through introducing TiO_2 in acetylene carbon black-graphite composite electrode. *Thin Solid Films* **2020**, *706*, 138042.
(26) Younas, M.; Gondal, M.; Dastageer, M.; Harrabi, K. Efficient and cost-effective dye-sensitized solar cells using MWCNT-TiO_2 nanocomposite as photoanode and MWCNT as Pt-free counter electrode. *Sol. Energy* **2019**, *188*, 1178−1188.
(27) Dwivedi, N.; et al. Understanding the Role of Nitrogen in Plasma-Assisted Surface Modification of Magnetic Recording Media with and without Ultrathin Carbon Overcoats. *Sci. Rep.* **2015**, *5*, 7772.
(28) Dager, A.; Uchida, T.; Maekawa, T.; Tachibana, M. Synthesis and characterization of mono-disperse carbon quantum dots from fennel seeds: Photoluminescence analysis using machine learning. *Sci. Rep.* **2019**, *9* (1), 14004.
(29) Dwivedi, N.; Yeo, R. J.; Satyanarayana, N.; Kundu, S.; Tripathy, S.; Bhatia, C. S.; et al. Understanding the role of nitrogen in plasma-assisted surface modification of magnetic recording media with and without ultrathin carbon overcoats. *Sci. Rep.* **2015**, *5* (1), 7772.
(30) Zhou, L.; et al. Thermodynamically and Dynamically Boosted Electrocatalytic Iodine Conversion with Hydroxyl Groups for High-Efficiency Zinc−Iodine Batteries. *ACS Appl. Mater. Interfaces* **2024**, *16*, 53881−53893.
(31) Qiu, C.; Jiang, L.; Gao, Y.; Sheng, L. Effects of oxygen-containing functional groups on carbon materials in supercapacitors: A review. *Mater. Des.* **2023**, *230*, 111952.
(32) Wang, S.; Nam, H.; Gebreegziabher, T. B.; Nam, H. Adsorption of acetic acid and hydrogen sulfide using NaOH impregnated activated carbon for indoor air purification. *Eng. Rep.* **2020**, *2* (1), No. e12083.
(33) Riyanto, C. A.; Ampri, M. S.; Martono, Y. Synthesis and characterization of nano activated carbon from annatto peels (Bixa orellana L.) viewed from temperature activation and impregnation ratio of H_3PO_4. *Eksakta: J. Sci. Data Anal.* **2020**, *20*, 44−50.
(34) Wang, B.; Xin, H.; Li, X.; Cheng, J.; Yang, G.; Nie, F.; et al. Mesoporous CNT@ TiO2-C nanocable with extremely durable high rate capability for lithium-ion battery anodes. *Sci. Rep.* **2014**, *4* (1), 3729.
(35) Kim, S.-G.; Park, O.-K.; Lee, J. H.; Ku, B.-C. Layer-by-layer assembled graphene oxide films and barrier properties of thermally reduced graphene oxide membranes. *Carbon Lett.* **2013**, *14*, 247−250.
(36) Lota, G.; et al. The application of activated carbon modified by ozone treatment for energy storage. *J. Solid State Electrochem.* **2016**, *20*, 2857−2864.
(37) Lee, J. S.; You, K. H.; Park, C. B. Highly photoactive, low bandgap TiO_2 nanoparticles wrapped by graphene. *Adv. Mater.* **2012**, *24*, 1084−1088.
(38) Wang, M.; Grätzel, C.; Zakeeruddin, S. M.; Grätzel, M. Recent developments in redox electrolytes for dye-sensitized solar cells. *Energy Environ. Sci.* **2012**, *5*, 9394−9405.
(39) Noorasid, N. S.; Arith, F.; Mustafa, A. N.; Azam, M. A.; Suhaimy, S. H. M.; Al-Ani, O. A. Effect of Low Temperature Annealing on Anatase TiO2 Layer as Photoanode for Dye-Sensitized Solar Cell. *Przegl. Elektrotech.* **2021**, *97* (10), 12−16.
(40) Rajaramanan, T.; Heidari Gourji, F.; Velauthapillai, D.; Ravirajan, P.; Senthilnanthanan, M.; Thirumurugan, A. Enhanced Photovoltaic Properties of Dye-Sensitized Solar Cells through Ammonium Hydroxide-Modified (Nitrogen-Doped) Titania Photoanodes. *Int. J. Energy Res.* **2023**, *2023*, 1090174.
(41) Rajaramanan, T.; et al. Cost effective solvothermal method to synthesize Zn-Doped TiO2 nanomaterials for photovoltaic and photocatalytic degradation applications. *Catalysts* **2021**, *11*, 690.
(42) Wei, W.; Sun, K.; Hu, Y. H. An efficient counter electrode material for dye-sensitized solar cells—flower-structured 1T metallic phase MoS_2. *J. Mater. Chem. A* **2016**, *4*, 12398−12401.
(43) Gao, R.; Cui, Y.; Liu, X.; Wang, L. Multifunctional interface modification of energy relay dye in quasi-solid dye-sensitized solar cells. *Sci. Rep.* **2014**, *4* (1), 5570.

https://doi.org/10.1021/acsomega.4c09967
ACS Omega 2025, 10, 39415−39425

(44) Yue, G.; et al. Nickel sulfide films with significantly enhanced electrochemical performance induced by self-assembly of 4-amino-thiophenol and their application in dye-sensitized solar cells. *RSC Adv.* **2014**, *4*, 64068−64074.
(45) Tangtrakarn, A.; et al. High stability arc-evaporated carbon counter electrodes in a dye sensitized solar cell based on inorganic and organic redox mediators. *Diamond Relat. Mater.* **2019**, *97*, 107451.
(46) Weerasinghe, M. I. U.; Kumarage, P. M. L.; Amarathunga, I. G. K. D.; Bandara, T. M. W. J.; Velauthapillai, D.; Karunarathne, B. C.; Punniamoorthy, R.; Rajapakse, R. M. G.; Kumara, G. R. A. Active Carbon Derived from Rice Husk as Sustainable Substitutes for Costly Platinum Electrodes in Dye-Sensitized Solar Cells. *J. Sci.: Adv. Mater. Devices* **2024**, *9* (3), 100749.

https://doi.org/10.1021/acsomega.4c09967
ACS Omega 2025, 10, 39415−39425